





## Article

# Detecting and Mapping Peatlands in the Tibetan Plateau Region Using the Random Forest Algorithm and Sentinel Imagery

Zihao Pan <sup>1,2,3</sup>, Hengxing Xiang <sup>2,\*</sup> , Xinying Shi <sup>2</sup>, Ming Wang <sup>4</sup>, Kaishan Song <sup>2</sup> , Dehua Mao <sup>2</sup>   
and Chunlin Huang <sup>1,5</sup> 

- <sup>1</sup> International Research Center of Big Data for Sustainable Development Goals, Beijing 100094, China  
<sup>2</sup> State Key Laboratory of Black Soils Conservation and Utilization, Northeast Institute of Geography and Agroecology, Chinese Academy of Sciences, Changchun 130102, China  
<sup>3</sup> Key Laboratory of Sustainable Forest Ecosystem Management-Ministry of Education, School of Forestry, Northeast Forestry University, Harbin 150040, China  
<sup>4</sup> College of Resources and Environment, Anhui Agricultural University, Hefei 230036, China  
<sup>5</sup> Northwest Institute of Eco-Environment and Resources, Chinese Academy of Sciences, Lanzhou 730000, China  
\* Correspondence: xianghengxing@iga.ac.cn

**Abstract:** The extensive peatlands of the Tibetan Plateau (TP) play a vital role in sustaining the global ecological balance. However, the distribution of peatlands across this region and the related environmental factors remain poorly understood. To address this issue, we created a high-resolution (10 m) map for peatland distribution in the TP region using 6146 Sentinel-1 and 23,730 Sentinel-2 images obtained through the Google Earth Engine platform in 2023. We employed a random forest algorithm that integrated spatiotemporal features with field training samples. The overall accuracy of the peatland distribution map produced is high, at 86.33%. According to the classification results, the total area of peatlands on the TP is 57,671.55 km<sup>2</sup>, and they are predominantly located in the northeast and southwest, particularly in the Zoige Protected Area. The classification primarily relied on the NDVI, NDWI, and RVI, while the DVI and MNDWI were also used in peatland mapping. B11, B12, NDWI, RVI, NDVI, and slope are the most significant features for peatland mapping, while roughness, correlation, entropy, and ASM have relatively slight significance. The methodology and peatland map developed in this work will enhance the conservation and management of peatlands on the TP while informing policy decisions and supporting sustainable development assessments.

**Keywords:** peatlands; random forest; time-series Sentinel-1 and -2 images; Google Earth Engine; Tibetan Plateau



Academic Editors: Ronghai Hu, Xiaoning Song, Fangcheng Zhou and Wenchao Han

Received: 3 December 2024

Revised: 10 January 2025

Accepted: 13 January 2025

Published: 15 January 2025

**Citation:** Pan, Z.; Xiang, H.; Shi, X.; Wang, M.; Song, K.; Mao, D.; Huang, C. Detecting and Mapping Peatlands in the Tibetan Plateau Region Using the Random Forest Algorithm and Sentinel Imagery. *Remote Sens.* **2025**, *17*, 292. <https://doi.org/10.3390/rs17020292>

**Copyright:** © 2025 by the authors. Licensee MDPI, Basel, Switzerland. This article is an open access article distributed under the terms and conditions of the Creative Commons Attribution (CC BY) license (<https://creativecommons.org/licenses/by/4.0/>).

## 1. Introduction

Peatlands are vital wetland ecosystems that play crucial roles in carbon sequestration, biodiversity support, and water cycle regulation [1–3]. They are also essential in mitigating climate change impacts [4]. The peatland ecosystems are threatened by natural disasters, including landslides and fires, as well as human activities such as drainage, cultivation, overgrazing, and infrastructure development. These threats lead to the decline of peatland areas and degradation of their functions [5]. The Tibetan Plateau (TP) comprises approximately 49% of China's entire peatland acreage [6] and 68% of its total peatland carbon reserves [5]. Previous studies have provided valuable datasets of TP peatlands [7,8]. However, these datasets are either outdated or insufficient for precise peatland recognition

and management. This is primarily due to limitations in spatial resolution, scale consistency, and differentiation of peatland types [7,8]. Consequently, the precise distribution of TP peatlands had not been accurately depicted by the existing datasets. Considering the growing necessity for precise quantification of peatland emissions, as well as the execution of restoration, rehabilitation, and rewetting initiatives, reliable peatland maps of the TP are urgently needed. Such maps are vital for comprehending the scope and status of peatlands and for mitigating further ecosystem degradation.

Traditional mapping methods based on the manual delineation of aerial photography have been used to determine peatland boundaries and distribution [9,10]. In contrast, digital mapping technologies offer a more economical, objective, and precise approach. These technologies facilitate the identification of threatened areas and support peatland resource protection [11]. Optical satellite data are widely used in mapping projects [12]. The use of Sentinel-1 and Sentinel-2 imagery, when combined with random forest (RF) algorithms, has been shown to be effective in extracting detailed characteristics of peatlands. It also enhances the precision of their boundaries and provides comprehensive descriptions of their spatial distribution [13]. The fine spatial resolution and dense temporal coverage of Sentinel-1 and -2 imagery also capture the seasonal variations in peatlands [14]. Previous studies have successfully used Sentinel-1 and Sentinel-2 data to map peatlands in central Estonia and Ireland [13–15]. Thus, the application of Sentinel-1 and -2 imagery for peatland mapping has proven to be feasible and effective. However, challenges remain due to the spectral similarity of peatlands with other wetland types, and the spatial heterogeneity in moisture content, vegetation density, and peat layer thickness [16]. These complicate the large-scale delineation of peatlands using satellite imagery [11]. With technological advancements, peatland mapping using machine learning techniques has increased [17,18].

Various machine learning algorithms, such as support vector machine (SVM), RF, and deep learning, have enabled the rapid mapping of wetlands globally. By addressing overfitting risks and the covariance of interdependent variables [19,20], the RF algorithm demonstrates a more robust fitting effect compared to other methods [21]. Synthetic aperture radar (SAR) data have also been used to supplement optical satellite data in the machine learning algorithm-based mapping of peatland-related land use and land cover change (LULC). Melton et al. (2022) successfully used Sentinel-1 InSAR on the Google Earth Engine (GEE) to identify and map global peatland distribution, demonstrating the potential of SAR data in peatland monitoring [16]. However, existing studies often rely on hydrological, soil, and topographical information for classification, making it challenging to identify hidden peatlands. The objective of this research was to promote peatland identification by employing the GEE in conjunction with Sentinel-1 and Sentinel-2 data to create an advanced classification model using an object-oriented RF methodology. This model incorporated an integrated indicator system that comprises climatic, topographic, and hydrologic characteristics. The resultant model was used to delineate the distribution of peatlands on the TP for 2023. By integrating SAR time-series data from Sentinel-1 with multispectral data from Sentinel-2, we aimed to accurately identify the peatland distribution. This was achieved through the use of multisource remote-sensing data and the GEE platform to develop a feature vector set that included various spatiotemporal attributes of vegetation, soil, and hydrology. The combination of the GEE with RF algorithms can facilitate the extraction of climatic parameters distinguishing peatlands from nonpeat marshes, which are herbaceous wetlands, woody wetlands, and other types of wetlands that are not classified as peatlands. Furthermore, the integration of time-series imagery from Sentinel-1 and Sentinel-2 established a rapid, reliable, and automated methodology for mapping peatlands, ultimately allowing for the swift and precise mapping of peatland distribution [22].

The TP, often referred to as the Third Pole, is an ecologically significant region hosting vast peatlands that contribute to the global ecological balance. Due to their sensitivity to environmental changes, these peatlands require vigilant protection and sustainable management [23]. Additionally, the unique geography and climate of the TP heightens the risk of peatland degradation in this area [24]. The regional peatland deterioration, attributable to anthropogenic activities such as drainage, peat extraction, and overgrazing, alongside the impacts of global climate change, has markedly influenced carbon emission fluxes and storage capacities. This degradation introduces uncertainties into the global greenhouse gas emissions and carbon sequestration calculations regarding peatlands, thereby exacerbating the challenges associated with climate change. The lack of accurate peatland data has led to a lag in research on a range of peatland issues on the TP. Current research on peatlands on the TP is limited to the northeastern and central permafrost peatlands [6,25]. Comprehensive mapping of peatlands across the entire plateau is, therefore, crucial to a better understanding of their distribution and dynamics.

In response to these challenges, this work uses the RF algorithm and a combination of Sentinel-1 and -2 imagery to accurately and comprehensively map the distribution of TP peatlands. The specific objectives of the current work are as follows: (1) to integrate time-series Sentinel-1 and -2 imagery with indicators representing vegetation, hydrology, and soil characteristics to construct an index system for peatland mapping and to use the RF algorithm to map the spatial distribution of peatlands; (2) to assess the accuracy of the generated maps and compare them with other available products; and (3) to analyze the spatial distribution of peatlands on the TP and evaluate the applicability of the chosen method.

## 2. Materials and Methods

### 2.1. Study Area

The Tibetan Plateau (TP) is in southwestern China (25°59'26"–40°1'6"N, 73°18'52"–104°46'59"E) [26], with an east–west length of approximately 2800 km and a north–south breadth of approximately 300–1500 km, covering a total area of approximately 2.5 million km<sup>2</sup> (Figure 1). The TP is the source area of major rivers in the surrounding areas. The TP predominantly features an alpine climate, which is characterized by the presence of perennial glaciers and snow in numerous regions. This climate is marked by significant diurnal and seasonal temperature variations, with long, cold winters and short, cool summers [27]. Its climate is influenced by the westerlies, the East Asian summer monsoon, and the South Asian summer monsoon [27]. Annual precipitation ranges from 200 mm (in the northwest of the TP, which is where the desert is) to 2000 mm (in the southeast of the TP, which is affected by the Indian Ocean southwest monsoon), and annual average temperatures vary from −6 °C (at mountaintops and high elevations) to 20 °C (in the southeast of the TP) [27]. The TP contains 41 national wetland conservation areas, and 7 of them are Ramsar sites, indicating their invaluable ecological contributions. The Yellow River Shouqu Protected Area (YSPA), Serinco Protected Area (SPA), Gongma Protected Area (GPA), and Zoige Protected Area (ZPA) are four representative Ramsar sites on the TP. The TP accumulated approximately 1.49 Pg of carbon in peat, accounting for 68% of the total C reserves in Chinese peatlands [27]. The boundary of the TP used in this study is obtained from the Third Pole Environment Data Center [26].

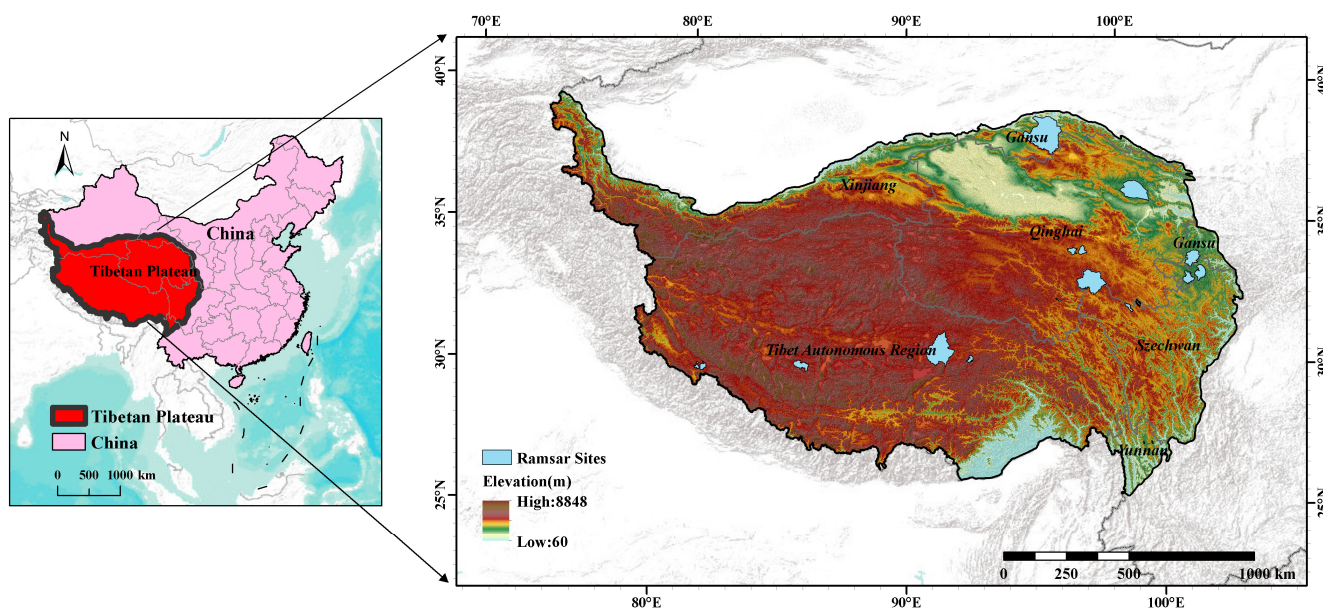


**Figure 1.** Geographic location and topography of the Tibetan Plateau in this study.

## 2.2. Datasets

### 2.2.1. Satellite Images and Preprocessing

The Sentinel-1 and -2 imagery, renowned for their high spatial and temporal resolution, form the basis of the spatiotemporal data used in this study. Dual-polarized vertical emission and vertical reception bands (VV) and vertical emission and horizontal reception bands (VH) of Sentinel-1 SAR GRD images used in this study have a spatial resolution of 10 m and a revisit interval of 12 days. Sentinel-2 offers a multispectral instrument with a spatial resolution of 10 m for visible and near-infrared bands, and 20 m for shortwave infrared bands, with a revisit cycle of 5 days. Multi-feature-based wetland detection was conducted using Sentinel-1 remote-sensing images and complemented with Sentinel-2 multispectral imagery. The Sentinel-1 and -2 data used in this work were collected and preprocessed on the GEE platform. The Sentinel-1 GRD dataset used in this study had been preprocessed, including de-distortion, radiometric correction, and terrain correction. The Sentinel-2 MSI dataset had been ortho-corrected and geometrically fine-corrected. A total of 29,876 Sentinel-1 and -2 surface reflectance images in the TP region for the period of January–December 2023 were acquired, comprising 6146 Sentinel-1 Ground Range Detected images and 23,730 Sentinel-2 multispectral instrument images. Figure 2a,b display the spatial distribution of high-quality imaging observations (have less than 20% cloud coverage and are free from significant noise or artifacts) on the TP in 2023 for Sentinel-1 and -2, respectively. More than 80% of the pixels were obtained over 50 Sentinel-1 observations, and more than 60% were obtained over 40 high-quality Sentinel-2 observations. The total number of Sentinel images available in each month is illustrated in Figure 2c,d. Sentinel-1 image quantities were all more than 459 each month, with a maximum of 582 in January; Sentinel-2 image quantities were all more than 975 each month, with a maximum of 2927 in November. The 30 m spatially resolved digital elevation model provided by the space Shuttle Radar Topography Mission (SRTM) was resampled to a 10 m DEM through the GEE platform using a bilinear interpolation algorithm to generate topographic information, including elevation and slope (Figure 1).

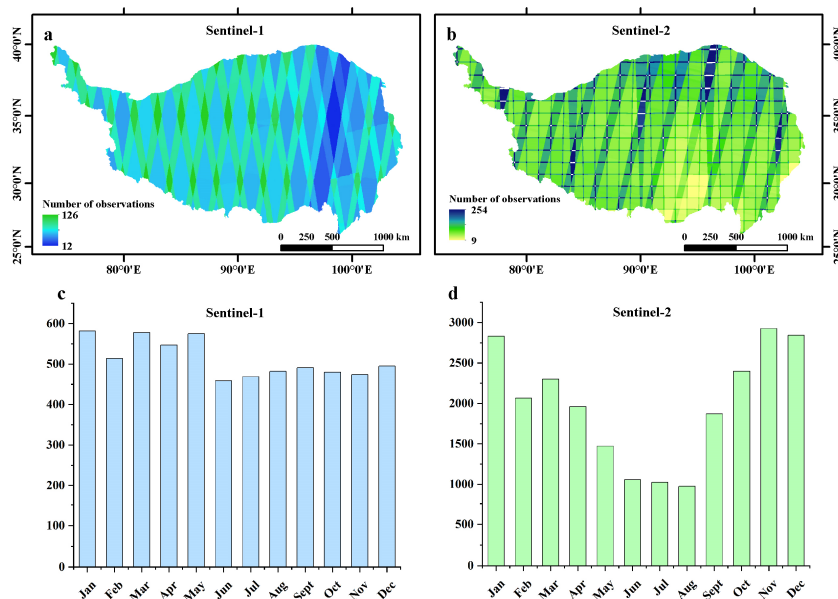


**Figure 2.** Spatial distributions of all available observations over the Tibetan Plateau in 2023 by Sentinel-1 (a) and Sentinel-2 (b), with histograms showing the monthly image acquisition numbers for Sentinel-1 (c) and Sentinel-2 (d).

### 2.2.2. Training Sample Data

To map the peatlands, we conducted field studies using Aowi software V10.1.6 to select sample points, take photos, and record land cover types. The samples collected through field sampling and visual interpretation were subsequently validated and refined using Sentinel imagery from 2023 available on the GEE to ensure the accuracy of the samples [28]. In instances where sample data were insufficient, we supplemented the dataset with an additional 456 sample points, using a visual interpretation method based on high-resolution Sentinel-1 and Sentinel-2 imagery (Figure 3). These samples were instrumental in identifying key features for peatland classification and in automatically generating additional training samples. Specifically, 70% of these samples were randomly selected to create new training samples using the automatic sample generation method proposed in this work, while the remaining 30% were reserved for performance validation. All reference samples were used to train the classification model alongside the new training samples generated automatically.

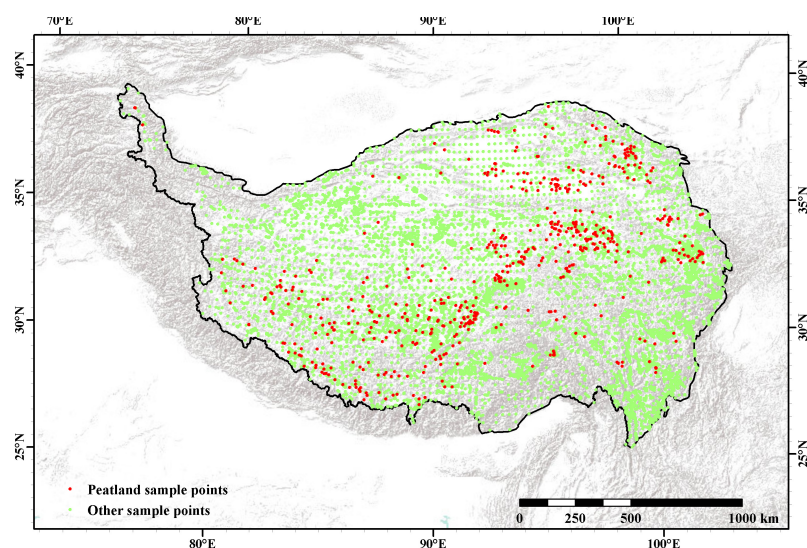


**Figure 3.** Distribution of sample points on the Tibetan Plateau.

### 2.2.3. Other Datasets

To facilitate a more accurate comparison with the current conditions and to enhance the results of this work, we selected the PEATMAP dataset [27] and the Peat-ML dataset [16] as reference maps for TP peatlands. We then compared and validated the predicted results from these datasets. Both additional datasets integrate information from digitized soil maps; wetland databases; and satellite imagery of swamps, marshes, bogs, and freshwater wetlands.

### 2.3. Methods

In this work, the TP wetlands were categorized into peatlands and nonpeat marshes based on the Ramsar Convention definition of wetlands and the wetland classification system used in various prior studies [29,30]. Other major land cover types were also categorized into woodland, grassland, water bodies, marsh, shrub, barren land, cropland, and built-up land. A hierarchical decision tree classification method was applied to map the different wetland categories in the study area, from which peatlands were identified. The peatland mapping process was divided into four main parts: extraction and selection of spatiotemporal features, automatic generation of training samples, peatland mapping using the RF classification method, and accuracy assessment (Figure 4).

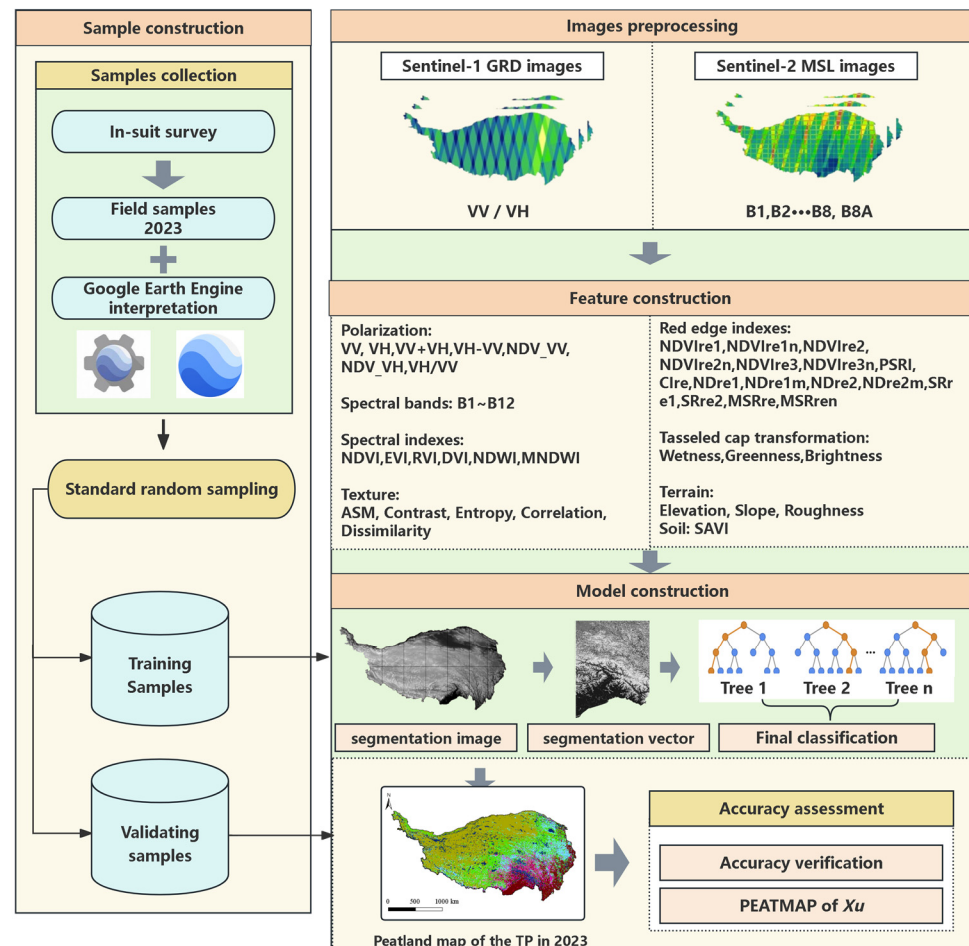


**Figure 4.** The general framework of the study in this work.

#### 2.3.1. Extraction and Selection of Spatiotemporal Features

Peatlands are characterized by an elevated organic matter content, a loose soil structure, and high moisture levels, which contribute to their distinctive features in both radar and optical imagery [11]. Specifically, radar imagery often reveals high backscattering

coefficients for peatlands, while optical imagery typically depicts them as darker brown with lower reflectance values [11]. These distinctions serve as primary differentiators between peatlands and nonpeat marsh environments [31]. However, the differentiation between peatlands and grasslands in radar and optical images is based on their spectral, textural, and thermal infrared characteristics, which complicates effective classification [32]. Consequently, a comprehensive set of 41 spatial and temporal variables was developed for peatland mapping in this study, aimed at accurately differentiating peatlands from other analogous land cover categories (Table 1). Various spatial variables were derived from the 2023 Sentinel-1 and -2 composite imagery, which included 13 spectral bands, 5 polarization indexes, 6 spectral indexes, 16 red-edge indexes, and 2 additional spectral indexes specific to the Sentinel-1 and -2 imagery. These spectral bands and indices have been proven to be proficient in distinguishing peatlands from nonpeat marsh areas, grasslands, and other land types [28]. The spectral indexes were calculated according to the bands with the following Equations (1)~(6):

$$NDWI = \frac{\rho_{green} - \rho_{nir}}{\rho_{green} + \rho_{nir}} \quad (1)$$

$$NDVI = \frac{\rho_{nir} - \rho_{red}}{\rho_{nir} + \rho_{red}} \quad (2)$$

$$EVI = 2.5 \times \frac{\rho_{nir} - \rho_{red}}{\rho_{nir} + 6 \times \rho_{red} - 7.5 \times \rho_{blue} + 1} \quad (3)$$

$$DVI = \rho_{nir} - \rho_{red} \quad (4)$$

$$RVI = \frac{\rho_{nir}}{\rho_{red}} \quad (5)$$

$$MNDWI = \frac{\rho_{green} - \rho_{nir}}{\rho_{green} + \rho_{nir}} \quad (6)$$

where  $\rho_{nir}$ ,  $\rho_{green}$ ,  $\rho_{red}$ ,  $\rho_{swir}$ , and  $\rho_{blue}$  are the reflectance in the near-infrared, green, red, shortwave, and blue bands, respectively.

**Table 1.** Spatiotemporal features extracted in this work.

Feature Category		Feature Name (Number)	Data Source
Polarization	Polarization bands	VV, VH (2)	Sentinel-1
	Polarization indexes	VV+VH, VH-VV, NDV_VV, NDV_VH, VH/VV (5)	
Spectral	Spectral bands	B1~B12 (13)	Sentinel-2
	Spectral indexes	NDVI, EVI, RVI, DVI, NDWI, MNDWI (6)	
	Red-edge indexes	NDVire1, NDVire1n, NDVire2, NDVire2n, NDVire3, NDVire3n, PSRI, CIRE, NDre1, NDre1m, NDre2, NDre2m, SRre1, SRre2, MSRre, MSRren (16)	
	Tasseled cap transformation	Wetness, Greenness, Brightness (3)	
Soil	SAVI		
Texture	ASM, Contrast, Entropy, Correlation, Dissimilarity (5)		Sentinel-2
Terrain	Elevation, Slope, Roughness (3)		DEM
Temporal	SWO		Sentinel-1/2

Note: NDVI (Normalized Difference Vegetation Index), EVI (Enhanced Vegetation Index), RVI (Ratio Vegetation Index), DVI (Difference Vegetation Index), NDWI (Normalized Difference Water Index), MNDWI (Modified Normalized Difference Water Index), PSRI (Plant Senescence Reflectance Index), SAVI (Soil-Adjusted Vegetation Index), and ASM (Adobe Standard Material).

Furthermore, the soil moisture conditions and flooding frequency might contribute to peatland development. Consequently, we employed Sentinel-1 and -2 time-series images to calculate the annual NDWI, VV, and VH, along with the Otsu algorithm [33], to extract

flood frequency data (Table 1) throughout the year, thereby characterizing the spatial and temporal dynamics of surface water occurrence (SWO). Additionally, polarization features, such as VV and VH, were effective in distinguishing between peatlands and nonpeat marsh sites [16]. The distinctions in these features between different land types were expected to underscore the efficacy of remote-sensing classification techniques in differentiating peatlands from other land types, thereby validating our feature selections. Detailed information is shown in Table 1.

### 2.3.2. Random Forest for Peatland Mapping

The RF algorithm was used for initial land-type classification based on the spatiotemporal features and the training samples, as described in Section 2.2.2. RF was combined with various decision trees, and bootstrap sampling was obtained from the training set for decision tree generation. The performance of a single decision tree in the RF classification model is poor, and few samples can be selected from the sample set for stochastic feature extraction. Hence, using multiple decision trees improves classification accuracy [32]. We set the number of decision trees to 500 and used bootstrap resampling to randomly select  $k$  samples with replacement, creating a new training dataset. Simultaneously, a terminal node that appears in the optimal segmentation scenario is chosen from the random subset of mapping variables. The final classification is determined by majority voting among all the trees in the forest. Finally, in conjunction with the sample data, mixed multisource variables are fed into the RF model to identify potential wetland distributions, and the hyperparameters are constantly adjusted to optimize the model's accuracy.

### 2.3.3. Accuracy Assessment of Peatland Classification Results

The accuracy of the peatland map created for 2023 in the TP region was evaluated using a random sampling method. First, the classification process resulted in three wetland categories and six non-wetland categories. Next, we assigned 14,640 random samples to the corresponding sample sizes, generated random points within each category, and visually examined and interpreted each sample point using high-resolution GEE images. To assess the accuracy of the peatland spatial distribution and areas derived from the maps, we also compared the mapping results with the previous peatland datasets, PEATMAP and Peat-ML. Finally, to assess the accuracy of the results and calculate their standard errors, we selected producer accuracy (PA), user accuracy (UA), overall accuracy (OA), and Kappa Coefficient as the metrics to evaluate the classification results. Each object in the validation set is treated as a sample. OA represents the percentage of correctly identified objects, UA indicates the proportion of correctly classified parts in the classification result, and PA is the ratio of correctly classified objects to the total number of objects [28]. The relevant equations are as follows:

$$P_{OA} = \sum_{i=1}^n P_{ii} / P \quad (7)$$

$$P_{UA} = P_{ii} / P_{i+} \quad (8)$$

$$P_{PA} = P_{ii} / P_{+i} \quad (9)$$

$$\text{Kappa} = \frac{P \sum_{i=1}^n P_{ii} - \sum_{i=1}^n (P_i + P_{+i})}{P^2 - \sum_{i=1}^n (P_i + P_{+i})} \quad (10)$$

where  $P_{OA}$  represents overall accuracy,  $P_{UA}$  represents user accuracy,  $P_{PA}$  represents producer accuracy,  $P$  represents the total number of samples,  $P_{ii}$  represents the number of samples in the  $i$ th row and  $i$ th column of the error matrix,  $P_{+i}$  represents the total count of



the  $i$ th class in the categorization result,  $P_{i+}$  represents the total count of the  $i$ th class in the ground-truthing data, and  $n$  represents the number of classes.

### 3. Results

#### 3.1. Peatland Features

Figure 5 illustrates the spectral, radar, and terrain signature characteristics of various land types on the Tibetan Plateau (TP). Given the potential confusion between grassland (GL) and peatland (PL) in the imagery, we selected grassland to compare with peatland and nonpeat marsh (NPM), which is herbaceous wetlands, woody wetlands, and other types of wetlands that were not classified as peatland. The DVI values for peatlands were observed in the range of 0.05–0.09, while the RVI values varied from 1.29 to 1.58. Additionally, the MNDWI values were recorded between 0.12 and 0.21, the NDWI values ranged from 0.09 to 0.14, and the NDVI values fell within the range of 0.03–to–0.07. Figure 5 demonstrates clear distinctions among the different land types across all features analyzed. Notably, the RVI values (1.29 to 1.58) for peatlands are substantially higher than those of nonpeat marsh (0.77 to 0.88) and GL (approximately 0). Thus, RVI can serve as a critical reference metric for distinguishing peatlands from grasslands. Additionally, we observed that the MNDWI, NDWI, NDVI, VV, and VH values for peatlands and grasslands are overlapped, corroborating the notion that grassland is often misidentified as peatland. Furthermore, the values of these indices for grassland are substantially lower than those for nonpeat marsh, except for MNDWI. On the TP, the slope does not allow a proper distinction between the three land types.

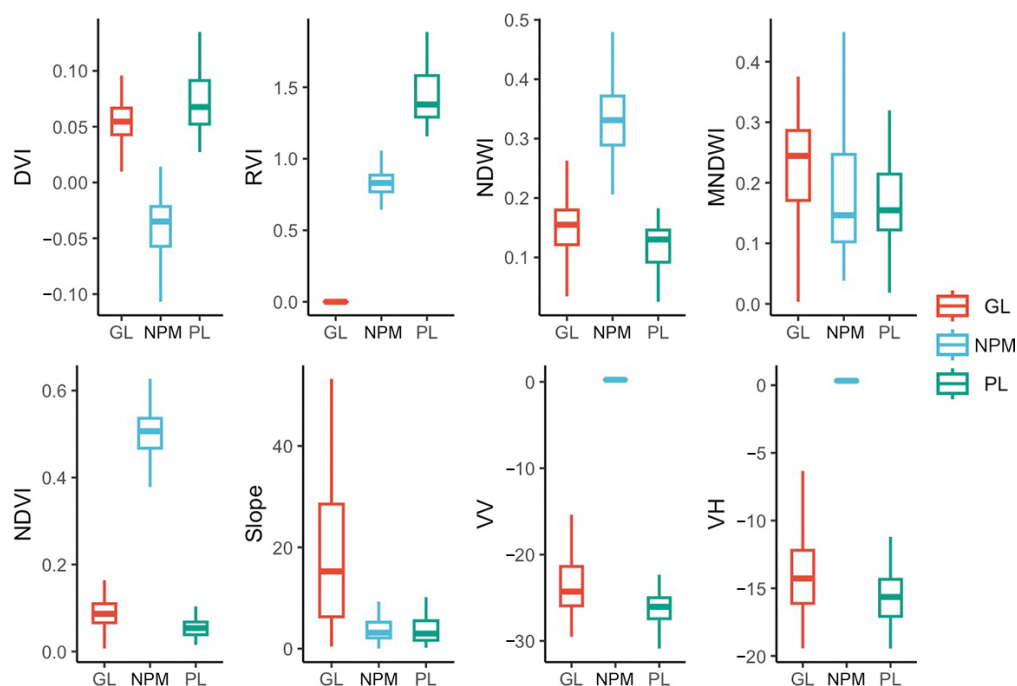


**Figure 5.** Comparison of typical characteristic variables between nonpeat marsh (NPM), grassland (GL), and peatland (PL) on the Tibetan Plateau.

We extracted 15 annual mean values for peatland, grassland, and nonpeat marsh land types using SAR image features from Sentinel-1 and spectral features from Sentinel-2 after preprocessing (Table 2). Subsequently, we calculated the differences between peatlands and other land types. Among the SAR-related features, the VV and VH polarizations effectively differentiated peatlands (26.03 and 15.60) from grasslands (23.57 and 13.69). Furthermore, the derived spectral data and features facilitate clear distinctions between

peatlands and nonpeat marsh areas. Specifically, the bands B6, B7, B8, B8A, B11, and B12 provide the information necessary for distinguishing between peatlands, grasslands, and nonpeat marsh. Consequently, annual mean parameters derived from SAR and spectral data can be employed to ascertain phenological characteristics, thereby enhancing the identification of peatlands.

**Table 2.** Differences between peatlands and other land types for the 15 annual mean characteristics.

Features	GL	PL	NPM
B1	0.24	0.24	0.25
B2	0.24	0.27	0.24
B3	0.25	0.28	0.25
B4	0.28	0.32	0.28
B5	0.30	0.34	0.30
B6	0.32	0.36	0.33
B7	0.33	0.37	0.35
B8	0.34	0.37	0.36
B8A	0.35	0.39	0.37
B9	0.30	0.32	0.32
B10	0.15	0.14	0.14
B11	0.38	0.37	0.35
B12	0.33	0.31	0.27
VV	23.57	26.03	24.96
VH	13.69	15.60	14.29

Note: PL stands for peatland. GL stands for grassland. NPM stands for herbaceous wetlands, woody wetlands, and other types of wetlands that are not classified as peatlands.

### 3.2. Classification Accuracy of Peatland Categories

The assessment demonstrated an overall classification accuracy of 86.33% and a Kappa of 0.72 for the generated 2023 TP peatland maps (Table 3). This result is highly consistent with the 761 validation samples. The UA and PA for peatlands were recorded at 89.84% and 78.96%, respectively. The classification accuracy for nonpeat marsh is also reliable (UA 83.99%, PA: 92.51%), indicating the robustness of the classification results.

**Table 3.** Evaluation of the accuracy of peatland classification results.

Data	Class	PL	NPM	Total	UA	Kappa	OA
2023	PL	274	31	305	89.84%	0.72	86.33%
	Non-PM	73	383	456	83.99%		
	Total	347	414	761	-		
	PA	78.96%	92.51%	-	-		

Note: PL stands for peatland. NPM stands for herbaceous wetlands, woody wetlands, and other types of wetlands that are not classified as peatlands.

### 3.3. Area and Distribution of Peatlands on the TP

Figure 6 illustrates the spatial distribution of peatlands on the TP as of 2023. The region's peatlands covered approximately 57,671.55 km<sup>2</sup> with evident spatial heterogeneity. The peatlands are primarily located in the northeastern and southwestern parts of the TP (Figure 6a). We selected several well-known international wetland reserves to analyze the spatial distribution of peatlands. The chosen protected wetland areas include the YSPA, SPA, GPA, and ZPA. In these internationally recognized protected wetland areas, the classification results indicated that peatlands were centralized. Notably, the ZPA encompasses the largest peatland area at 424.99 km<sup>2</sup> (Figure 6e), accounting for 0.74% of the total peatlands on the TP, while the GPA has the smallest area at 16.31 km<sup>2</sup> (Figure 6c), representing 0.02% of the total peatlands.

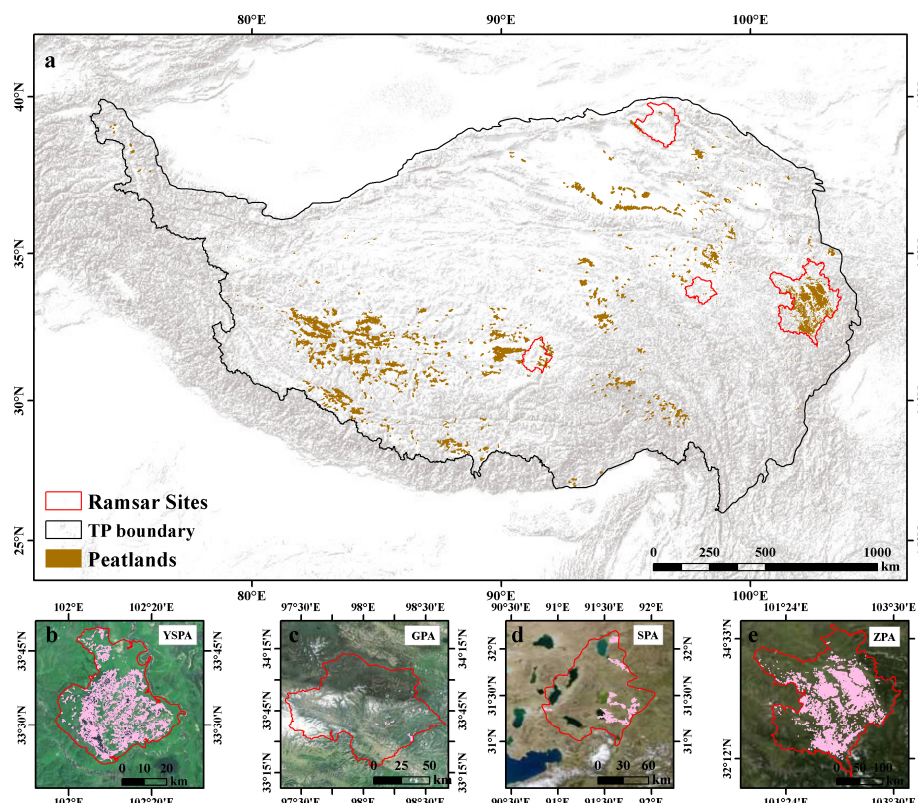


**Figure 6.** Distribution of peatlands on the Tibetan Plateau for 2023. (a) Spatial distribution of peatlands. (b–e) Distribution of peatlands (in pink) within major Ramsar sites: Yellow River Shouqu Protected Area (YSPA), Serinco Protected Area (SPA), Gongma Protected Area (GPA), and Zoige Protected Area (ZPA).

## 4. Discussion

### 4.1. Variable Importance of the Distribution of Peatlands

Figure 7 illustrates the degree to which various features contribute to the classification results. There are obvious differences in the factors influencing the distribution of TP peatlands. The most critical factors are B11 and B12, accounting for 5.28% and 5.16%. NDWI, RVI, NDVI, and slope also play important roles in the classification, accounting for 4.44%, 3.79%, 3.74%, and 3.22%, respectively. The roughness, conversely, had the smallest effect on peatland distribution, accounting for only 0.58%.

NDWI, RVI, NDVI, and slope are the key variables affecting peatland distribution in this work. This finding aligns with previous descriptions in the literature [34]. Because the NDWI and NDVI are the main indicators of surface water bodies, we speculate that the distribution of peatlands is also correlated with surface water bodies. We found that the mean annual precipitation was only around 400 mm in the ZPA, but the soil moisture index was between 1.8 and 2.0 [6], which was the highest in the TP peatland region. The high soil moisture is potentially due to its low evaporation resulting from a difficult runoff and low temperature and explains why the ZPA has the largest and most developed peatlands on the TP.

The thickness of the active layer may be another key factor influencing peatland distribution on the TP [35]. The thickness is critical for peatland development and expansion, as peatlands usually form in alpine zones where the active layer is less than 2.3 m thick [35]. This phenomenon may be related to the impermeability of the permafrost soil in alpine zones, which inhibits water infiltration and favors surface water accumulation. Alpine peatlands are sustained by perennial inflows of precipitation or groundwater, which may come from rainfall, snow-melt, or, in some cases, glaciers. We also found that slope had a

significant influence on peatland distribution. Our results indicate that the spatial distribution of peatlands is in flat areas with low slopes ( $<7^\circ$ ), between 4000 and 5000 m above sea level. This distribution pattern aligns with observations made in other alpine peatlands [7]. We hypothesize that the main factor contributing to this distribution is the higher soil water saturation in flat areas compared to steeper regions, which is crucial for peatland development. In summary, a complex interaction between climatic and topographic factors ultimately determines the distribution of peatlands on the TP.

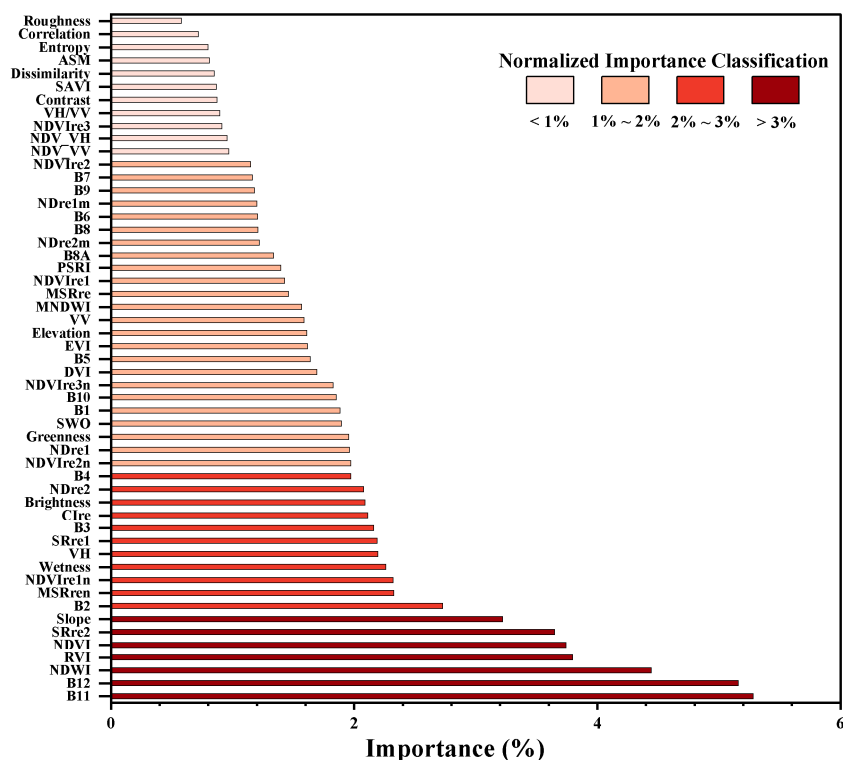
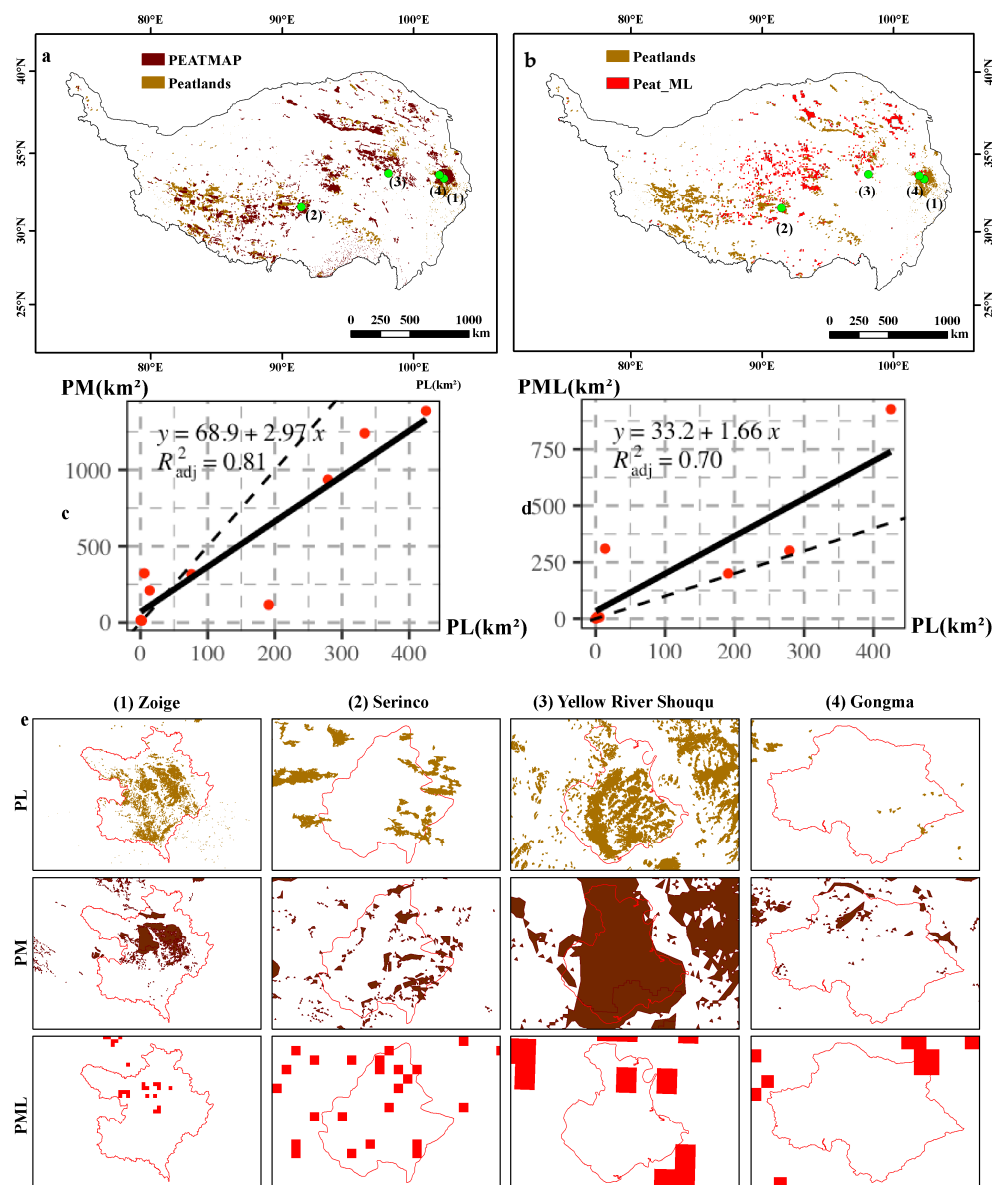


Figure 7. Order of feature importance for peatland mapping.

#### 4.2. High-Resolution Peatland Mapping Outcomes for the Tibetan Plateau

Figure 8 compares the peatland (PL) map generated in this work with the PEATMAP (PM) and Peat-ML (PML) datasets. The total area of peatland identified in this work was 57,671.55 km<sup>2</sup>, while the PM estimated the peatland area to be 55,683.80 km<sup>2</sup>. The areal regression curve for PL with the PM demonstrates a high degree of agreement between our results and the dataset ( $R^2 = 0.81$ ) (Figure 8a). Compared to the PM, this work presents an updated peatland map for 2023, featuring a finer spatial resolution of 10 m. The PM was compiled from multiple data sources and is, therefore, less accurate because the different data sources are a collection of wetland information from different time periods [36]. For instance, the ZPA peatlands are in regions characterized by slopes of less than  $5^\circ$ . However, the PM forecasts the presence of peatlands on slopes reaching up to  $10^\circ$ . Such steep inclines are generally not favorable for the accumulation of water, which is essential for sustaining the water table conditions necessary for peatland formation [37]. These observations underscore the constraints of the PM predictions within the TP region and emphasize the necessity for ground-truthing the projected maps. We also conducted separate comparisons with PML (Figure 8b). The area regression curve generated by PML with PL demonstrates a good consistency with our results ( $R^2 = 0.70$ ). The overall area predicted by our results is greater than that of PML, and there are two primary reasons for this discrepancy: First, PML, a wetland map developed using survey data from various sources and remote sensing, does not include many of the already-identified TP peatland

study sites [16]. Second, the observed area differences can be attributed to variations in data generation methods. Additionally, PML often fails to provide accurate predictions for many locations where peatlands have been identified, underestimating the extent of peatlands in the TP region. Because this work uses a map simulation based on actual peatlands as the sample points, the results are more consistent with the true peatland distribution.



**Figure 8.** Comparison of our peatland map with other peatland maps. (a,b) compare our result (PL) with peatland datasets PEATMAP (PM) and Peat-ML (PML) for peatland distribution on the TP, respectively. (c,d) show the correlation between the peatland areas ( $\text{km}^2$ ) of protected peatland areas in our result (PL) and those in the PM and PML, respectively. (e) presents the comparison of our results (PL) with the PM and PML in four Ramsar sites: (1) Zoige Protected Area (ZPA), (2) Serinco Protected Area (SPA), (3) Yellow River Shouqu Protected Area (YSPA), and (4) Gongma Protected Area (GPA).

#### 4.3. Implications of Peatland Mappings

In this work, the TP peatlands were mapped with a resolution of 10 m. The high-resolution peatland distribution product has a wide range of potential applications in scientific research and sustainable management, including biodiversity conservation, carbon stock assessment, and carbon sink estimation. For instance, detailed information about the spatial distribution of peatlands can enhance our understanding of their ecological

functions and services, which is critical for carbon sink studies of terrestrial ecosystems. Additionally, this information can be used to evaluate the conservation status and transformation of peatlands, providing valuable insights for the sustainable planning and management of peat resources. Furthermore, detailed maps contribute to the restoration and development of peat resources in degraded peatlands and support informed decision making regarding peatland conservation and restoration. However, the current products remain insufficient. Due to various factors, it is currently impossible to study the peatlands in the western TP.

Our TP peatland map also has certain limitations. We have not explored the possibilities offered by many other algorithms. For instance, deep learning algorithms show great potential for processing large-scale remote-sensing data, being able to extract features from complex images and build classification and regression models. In peatland mapping, these deep learning algorithms could help to distinguish peatlands from other wetland types, especially when their spectral features are similar [15]. Future research should explore how deep learning algorithms can be utilized to improve the accuracy and efficiency of peatland mapping. Also, our model does not account for the presence of snow and numerous glaciers covering this region, which may limit its effectiveness in assessing peatlands influenced by glaciers and snow. Our model is predicated on environmental factors such as geomorphological characteristics, vegetation types, soil moisture conditions, and climate-related factors. However, peatlands can also modify their surrounding environment (for instance, by accumulating peat in depressions or altering the hydrological dynamics of vegetation), thereby complicating the differentiation between causal and consequential relationships regarding peatland distribution and environmental factors. Furthermore, our methodology is less prescriptive compared to that of Hugelius et al. [38], who defined peatlands based on the soil carbon content at specific locations. Consequently, the peatland distributions generated from our simulations diverge from those established through carbon content criteria. Additionally, the RF algorithm used in this work identifies numerous key features from the data without a comprehensive understanding of the specific ecological processes that govern peatland formation and evolution. Therefore, future research should integrate process-based modeling to enhance our understanding of the changes in the extent of TP peatlands and the fluctuations in carbon stocks in response to climate change.

## 5. Conclusions

In this study, the Sentinel-1 and Sentinel-2 time-series images combined with vegetation, hydrology, and soil characteristics were used to map the peatlands on the Tibetan Plateau with the high resolution of 10 m. The integration of spatial and temporal features with an efficient method for automatic sample generation significantly enhanced the accuracy of peatland classification, achieving an overall accuracy of 86.33%. This result underscores the effectiveness of the random forest algorithm in distinguishing peatlands from nonpeat marsh areas, thereby facilitating a detailed analysis of peatland distribution. The accuracy assessment and comparison with existing datasets such as PEATMAP and Peat-ML revealed that our map provides a more accurate and up-to-date representation of peatlands on the Tibetan Plateau. Through a comprehensive analysis of the spatial distribution of peatlands, it is revealed that significant peatland concentrations are in key protected areas. Overall, the methodology and products developed in this study offer significant contributions to the conservation and management of peatlands on the Tibetan Plateau. They can also serve as a critical resource for assessing Sustainable Development Goal targets and support the development of more comprehensive peatland maps globally. Future research could explore the integration of additional environmental variables

and advanced machine learning techniques to further refine the accuracy and predictive capabilities of peatland mapping models.

**Author Contributions:** Methodology, Software, Writing—original draft, Z.P.; Conceptualization, Validation, Funding acquisition, Writing—review and editing, H.X.; Writing—review and editing, Validation, X.S.; Data curation, Validation, M.W.; Writing—review and editing, K.S.; Writing—review and editing, D.M.; Writing—review and editing, C.H. All authors have read and agreed to the published version of the manuscript.

**Funding:** This research was jointly funded by the National Natural Science Foundation of China: [U2243230, 42494821, 42330109], the “Young support talents program” from the Science and Technology Association of Jilin Province (2024–2026) to Hengxing Xiang (QT202417), and the Open Research Program of the International Research Center of Big Data for Sustainable Development Goals (CBAS2023ORP04).

**Data Availability Statement:** The original contributions presented in the study are included in the article, further inquiries can be directed to the corresponding author.

**Conflicts of Interest:** The authors declare that they have no known competing financial interests or personal relationships that could have appeared to influence the work reported in this paper.

## References

- Page, S.E.; Rieley, J.O.; Banks, C.J. Global and regional importance of the tropical peatland carbon pool. *Glob. Chang. Biol.* **2011**, *17*, 798–818. [[CrossRef](#)]
- Scharlemann, J.; Tanner, E.; Hiederer, R.; Kapos, V. Global soil carbon: Understanding and managing the largest terrestrial carbon pool. *Carbon Manag.* **2014**, *5*, 81–91. [[CrossRef](#)]
- Yu, Z.C. Northern peatland carbon stocks and dynamics: A review. *Biogeosciences* **2012**, *9*, 4071–4085. [[CrossRef](#)]
- Gorham, E. Northern Peatlands: Role in the Carbon Cycle and Probable Responses to Climatic Warming. *Ecol. Appl.* **1991**, *1*, 182–195. [[CrossRef](#)]
- Yang, G.; Peng, C.; Chen, H.; Dong, F.; Wu, N.; Yang, Y.; Zhang, Y.; Zhu, D.; He, Y.; Shi, S.; et al. Qinghai–Tibetan Plateau peatland sustainable utilization under anthropogenic disturbances and climate change. *Ecosyst. Health Sustain.* **2017**, *3*, e01263. [[CrossRef](#)]
- Sun, J.; Gallego-Sala, A.; Yu, Z. Topographic and climatic controls of peatland distribution on the Tibetan Plateau. *Sci. Rep.* **2023**, *13*, 14811. [[CrossRef](#)]
- Chen, H.; Yang, G.; Peng, C.; Zhang, Y.; Zhu, D.; Zhu, Q.; Hu, J.; Wang, M.; Zhan, W.; Zhu, E.; et al. The carbon stock of alpine peatlands on the Qinghai–Tibetan Plateau during the Holocene and their future fate. *Quat. Sci. Rev.* **2014**, *95*, 151–158. [[CrossRef](#)]
- Yao, L.; Zhao, Y.; Gao, S.; Sun, J.; Li, F. The peatland area change in past 20 years in the Zoige Basin, eastern Tibetan Plateau. *Front. Earth Sci.* **2011**, *5*, 271–275. [[CrossRef](#)]
- Cruickshank, M.M.; Tomlinson, R.W. Peatland in Northern Ireland: Inventory and prospect. *Ir. Geogr.* **1990**, *23*, 17–30. [[CrossRef](#)]
- Vitt, D.H.; Halsey, L.A.; Bauer, I.E.; Campbell, C. Spatial and temporal trends in carbon storage of peatlands of continental western Canada through the Holocene. *Can. J. Earth Sci.* **2000**, *37*, 683–693. [[CrossRef](#)]
- Minasny, B.; Berglund, Ö.; Connolly, J.; Hedley, C.; de Vries, F.; Gimona, A.; Kempen, B.; Kidd, D.; Lilja, H.; Malone, B.; et al. Digital mapping of peatlands—A critical review. *Earth-Sci. Rev.* **2019**, *196*, 102870. [[CrossRef](#)]
- Aitkenhead, M.J. Mapping peat in Scotland with remote sensing and site characteristics. *Eur. J. Soil Sci.* **2017**, *68*, 28–38. [[CrossRef](#)]
- Tampuu, T.; Praks, J.; Kull, A.; Uiboupin, R.; Tamm, T.; Voormansik, K. Detecting peat extraction related activity with multi-temporal Sentinel-1 InSAR coherence time series. *Int. J. Appl. Earth Obs. Geoinf.* **2021**, *98*, 102309. [[CrossRef](#)]
- Feng, M.; Qi, Q.; Dong, Y.; Zeng, L.; Zhang, X.; Liu, W.; Li, Y.; Wang, T.; Zhang, G. Monitoring Surface Deformation in Xi’an City from 2019 to 2022 Based on Sentinel-1A Data. *Northwest. Geol.* **2023**, *56*, 178–185.
- Habib, W.; Ingle, R.; Saunders, M.; Connolly, J. Quantifying peatland land use and CO<sub>2</sub> emissions in Irish raised bogs: Mapping insights using Sentinel-2 data and Google Earth Engine. *Sci. Rep.* **2024**, *14*, 1171. [[CrossRef](#)]
- Melton, J.R.; Chan, E.; Millard, K.; Fortier, M.; Winton, R.S.; Martín-López, J.M.; Cadillo-Quiroz, H.; Kidd, D.; Verchot, L.V. A map of global peatland extent created using machine learning (Peat-ML). *Geosci. Model Dev.* **2022**, *15*, 4709–4738. [[CrossRef](#)]
- DeLancey, E.R.; Kariyeva, J.; Bried, J.T.; Hird, J.N. Large-scale probabilistic identification of boreal peatlands using Google Earth Engine, open-access satellite data, and machine learning. *PLoS ONE* **2019**, *14*, e0218165. [[CrossRef](#)]
- O’Leary, D.; Brown, C.; Daly, E. Digital soil mapping of peatland using airborne radiometric data and supervised machine learning—Implication for the assessment of carbon stock. *Geoderma* **2022**, *428*, 116086. [[CrossRef](#)]
- Breiman, L. Random Forests. *Mach. Learn.* **2001**, *45*, 5–32. [[CrossRef](#)]

20. Merghadi, A.; Yunus, A.P.; Dou, J.; Whiteley, J.; ThaiPham, B.; Bui, D.T.; Avtar, R.; Abderrahmane, B. Machine learning methods for landslide susceptibility studies: A comparative overview of algorithm performance. *Earth-Sci. Rev.* **2020**, *207*, 103225. [CrossRef]
21. Li, L.; Zhou, B.; Liu, Y.; Wu, Y.; Tang, J.; Xu, W.; Wang, L.; Ou, G. Reduction in Uncertainty in Forest Aboveground Biomass Estimation Using Sentinel-2 Images: A Case Study of Pinus densata Forests in Shangri-La City, China. *Remote Sens.* **2023**, *15*, 559. [CrossRef]
22. Wang, M.; Mao, D.; Wang, Y.; Xiao, X.; Xiang, H.; Feng, K.; Luo, L.; Jia, M.; Song, K.; Wang, Z. Wetland mapping in East Asia by two-stage object-based Random Forest and hierarchical decision tree algorithms on Sentinel-1/2 images. *Remote Sens. Environ.* **2023**, *297*, 113793. [CrossRef]
23. Wang, P.; Wolf, S.A.; Lassoie, J.P.; Poe, G.L.; Morreale, S.J.; Su, X.; Dong, S. Promise and reality of market-based environmental policy in China: Empirical analyses of the ecological restoration program on the Qinghai-Tibetan Plateau. *Glob. Environ. Change* **2016**, *39*, 35–44. [CrossRef]
24. Shi, J.; Liu, W.; Li, R.; Wu, X.; Wu, T.; Zhao, L.; Ma, J.; Wang, S.; Xiao, Y.; Hu, G.; et al. Research Progress in the Field of Peatlands in 1990–2022: A Systematic Analysis Based on Bibliometrics. *Land* **2024**, *13*, 549. [CrossRef]
25. Li, Y.; Yu, Z.; Wang, M.; Li, H.; Sun, J.; Wang, S. Control of local topography and surface patterning on the formation and stability of a slope permafrost peatland at 4800-m elevation on the central Qinghai-Tibetan Plateau. *Ecol. Indic.* **2024**, *158*, 111475. [CrossRef]
26. Zhang, Y.; Li, B.; Liu, L.; Zheng, D. A discussion on the boundary and area of the Tibetan Plateau in China. *Geogr. Res.* **2002**, *21*, 1–8.
27. Yang, Y.; Hu, Z.; Lu, F.; Cai, Y.; Yu, H.; Guo, R.; Fu, C.; Fan, W.; Wu, D. Progress of Recent 60 Years' Climate Change and Its Environmental Impacts on the Qinghai-Xizang Plateau. *Plateau Meteorol.* **2022**, *41*, 1.
28. Xiang, H.; Xi, Y.; Mao, D.; Xu, T.; Wang, M.; Yu, F.; Feng, K.; Wang, Z. Modeling potential wetland distributions in China based on geographic big data and machine learning algorithms. *Int. J. Digit. Earth* **2023**, *16*, 3706–3724. [CrossRef]
29. Mao, D.; Wang, Z.; Du, B.; Li, L.; Tian, Y.; Jia, M.; Zeng, Y.; Song, K.; Jiang, M.; Wang, Y. National wetland mapping in China: A new product resulting from object-based and hierarchical classification of Landsat 8 OLI images. *ISPRS J. Photogramm. Remote Sens.* **2020**, *164*, 11–25. [CrossRef]
30. Gong, P.; Niu, Z.; Cheng, X.; Zhao, K.; Zhou, D.; Guo, J.; Liang, L.; Wang, X.; Li, D.; Huang, H.; et al. China's wetland change (1990–2000) determined by remote sensing. *Sci. China Earth Sci.* **2010**, *53*, 1036–1042. [CrossRef]
31. de la Barreda-Bautista, B.; Boyd, D.S.; Ledger, M.; Siewert, M.B.; Chandler, C.; Bradley, A.V.; Gee, D.; Large, D.J.; Olofsson, J.; Sowter, A.; et al. Towards a Monitoring Approach for Understanding Permafrost Degradation and Linked Subsidence in Arctic Peatlands. *Remote Sens.* **2022**, *14*, 444. [CrossRef]
32. Chrysafis, I.; Mallinis, G.; Gitas, I.; Tsakiri-Strati, M. Estimating Mediterranean forest parameters using multi seasonal Landsat 8 OLI imagery and an ensemble learning method. *Remote Sens. Environ.* **2017**, *199*, 154–166. [CrossRef]
33. Otsu, N. A Threshold Selection Method from Gray-Level Histograms. *IEEE Trans. Syst. Man Cybern.* **1979**, *9*, 62–66. Available online: <https://ieeexplore.ieee.org/document/4310076/authors#authors> (accessed on 29 September 2024). [CrossRef]
34. Pontone, N.; Millard, K.; Thompson, D.K.; Guindon, L.; Beaudoin, A. A hierarchical, multi-sensor framework for peatland sub-class and vegetation mapping throughout the Canadian boreal forest. *Remote Sens. Ecol. Conserv.* **2024**, *10*, 500–516. [CrossRef]
35. Squeo, F.A.; Warner, B.G.; Aravena, R.; Espinoza, D. Bofedales: High altitude peatlands of the central Andes. *Rev. Chil. Hist. Nat.* **2006**, *79*, 245–255. [CrossRef]
36. Xu, J.; Morris, P.J.; Liu, J.; Holden, J. PEATMAP: Refining estimates of global peatland distribution based on a meta-analysis. *Catena* **2018**, *160*, 134–140. [CrossRef]
37. Zhao, Y.; Tang, Y.; Yu, Z.; Li, H.; Yang, B.; Zhao, W.; Li, F.; Li, Q. Holocene peatland initiation, lateral expansion, and carbon dynamics in the Zoige Basin of the eastern Tibetan Plateau. *Holocene* **2014**, *24*, 1137–1145. [CrossRef]
38. Hugelius, G.; Loisel, J.; Chadburn, S.; Jackson, R.B.; Jones, M.; MacDonald, G.; Marushchak, M.; Olefeldt, D.; Packalen, M.; Siewert, M.B.; et al. Large stocks of peatland carbon and nitrogen are vulnerable to permafrost thaw. *Proc. Natl. Acad. Sci. USA* **2020**, *117*, 20438–20446. [CrossRef]

**Disclaimer/Publisher's Note:** The statements, opinions and data contained in all publications are solely those of the individual author(s) and contributor(s) and not of MDPI and/or the editor(s). MDPI and/or the editor(s) disclaim responsibility for any injury to people or property resulting from any ideas, methods, instructions or products referred to in the content.